Assessment of Fencing on the Orion Heatshield

Antonella I. Alunni[*] and Tahir Gökçen[†]
AMA Inc., NASA Ames Research Center, Moffett Field, CA 94035

This paper presents recession measurements of arc-jet test articles that simulate an ablator with gap filler and were exposed to various heating profiles. Results were used to derive empirically-based differential recession models used for the baseline sizing of the Orion block heatshield architecture. The profile test conditions represent different local flight environments associated with different regions of the heatshield. Recession measurements were collected during and after arc-jet tests, and the results were used to observe the heating profiles' effect on differential recession. Arc-jet tests were conducted at the Aerodynamic Heating Facility at NASA Ames Research Center.

Nomenclature

h_{ob} = mass-averaged total enthalpy (or bulk enthalpy), MJ/kg
h_{ocl} = centerline total enthalpy, MJ/kg
I = arc current, A
$\dot{m}$ = mass flow rate, kg/s
p_{midc} = arc-heater mid-column pressure, kPa
p_s = surface pressure, kPa
q_s = surface heat flux, W/cm^2
q_{HWFC} = hot-wall full-catalytic heat flux, W/cm^2
r_c = model corner radius, cm
V = arc voltage, V

I. Introduction

After successful completion of the Orion Exploration Flight Test 1 (EFT-1) in December 2014, the Orion program conducted various trade studies across subsystems to identify potential improvements for Orion's subsequent mission, Exploration Mission 1 (EM-1). The program concluded that a block heatshield architecture, comprising a tiled layout of molded Avcoat blocks, would be a more suitable thermal protection system (TPS) than the honeycomb Avcoat heatshield that was flown.[1] The molded Avcoat would facilitate greater control over manufacturing while granting higher confidence in the performance of Orion's TPS relative to the EFT-1 heatshield.

The tiled layout, which is designed to prevent adjacent blocks from contacting under thermal expansion, requires a gap filler to inhibit flow penetration between the molded Avcoat blocks. RTV-560 was ultimately selected as the gap filler for EM-1. Unlike the EFT-1 heatshield, which experienced fairly uniform recession rates between the honeycomb and the ablator, disparate recession rates between the gap filler and molded Avcoat is expected to produce differential recession in the EM-1 heatshield. Differential recession can be revealed as fencing in the event that the gap filler recedes slower than Avcoat or gapping in the event that the gap filler recedes faster than Avcoat. Differential recession at the block interfaces can pose risks such as augmented heating and earlier transition to turbulence. Given that low heating governs the latter part of the EM-1 trajectory and the gap filler is more robust than the ablator at relatively low surface temperatures, fencing is expected to dominate the surface response across the heatshield.

NASA's Mars Science Laboratory (MSL) TPS encountered analogous risks with its design, which consisted of tiled Phenolic Impregnated Carbon Ablator (PICA). Ultimately, high heating augmentation

---

[*] Research Scientist, MS 234-1, Member AIAA
[†] Senior Research Scientist, MS 230-2, Associate Fellow AIAA

was predicted for the leeward region of the heatshield.[2] However, this region was anticipated to have relatively high heat fluxes, thicker boundary layer, and gaps oriented nearly perpendicular to the flow, which naturally mitigate against the development of fencing. Nevertheless, the program investigated associated risks by analyzing the effects of fencing via computational fluid dynamics (CFD)[3] and arc-jet testing PICA with filled gaps in shear.[4]

For EM-1, capturing the coupled nature of fences and environments is important when considering the risks related to fencing. The development of fencing highly depends on the flight environment since recession rates vary with heating, pressure, and shear. At the same time, local heating environments depend on the fence height given that a protuberance can influence heating augmentation and transition to turbulence, which in turn affects downstream environments. So, sizing the updated Orion TPS architecture is achieved by using fencing inputs based on test results to generate local heating environments that depict the augmented heating distribution and transition effects across the heatshield.

To develop the fencing models required for sizing inputs, fencing was investigated via arc-jet tests in the Aerodynamic Heating Facility (AHF) using the 10-MW TP3 arc heater at NASA Ames Research Center (ARC). The primary objective of these tests was to obtain fencing profiles using flat-faced stagnation models for a wide range of heating profiles. Each heating profile was simulated through seven constant arc-heater conditions or steps. This paper specifically addresses the approaches and techniques used to characterize the surface response resulting from heating-profile tests to produce a set of differential recession profiles that inform fencing development.

II. Test Description

A. Target Heating Environments

Arc-jet tests were conducted for 10 different dual-pulse heating profiles representative of the Orion flight. The profiles were developed from the predictions of time-varying environments for two distinct entry interface (EI) guided trajectories. Each EI trajectory is portrayed by heating profiles that correspond to five different heatshield regions, ranging from high heating at the stagnation point to low heating at the leeward shoulder.

The continuous EI profiles were approximated by targeted stepwise heating profiles in the arc-jet tests. As illustrated in Figs. 1-2, every profile consisted of seven different steps: five steps of increasing then decreasing heat flux and pressure comprised the first pulse, one step of low heat flux and pressure comprised the dwell, and the last step of increased heat flux and pressure comprised the second pulse. The five EI2 profiles that were tested had the same heat flux and pressure targets as the set of five EI6 profiles. However, the EI6 profiles had a longer dwell time followed by a longer second pulse compared to EI2 profiles, resulting in 770-second durations for EI6 profiles and 560-second durations for EI2 profiles.

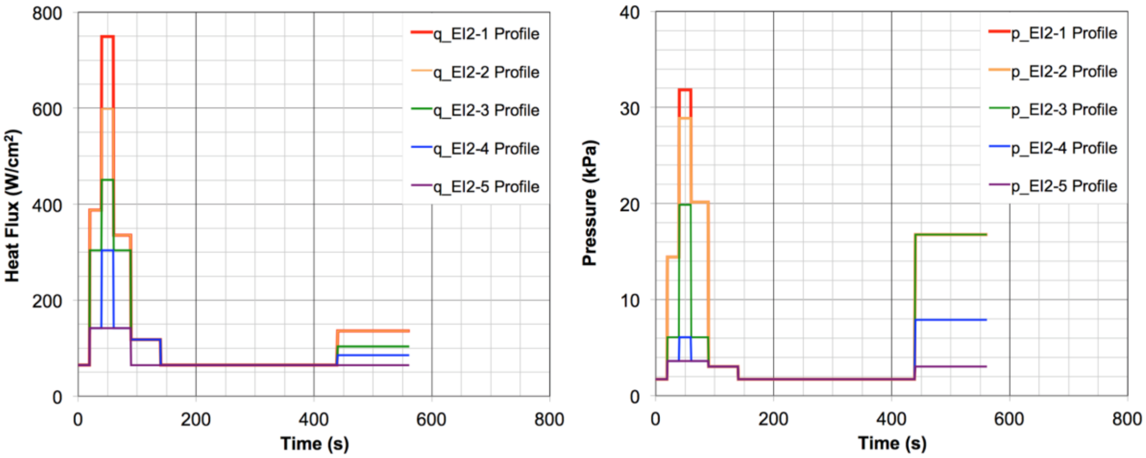

Figure 1. EI2 set of cold-wall heat flux and pressure profiles that were developed for testing.

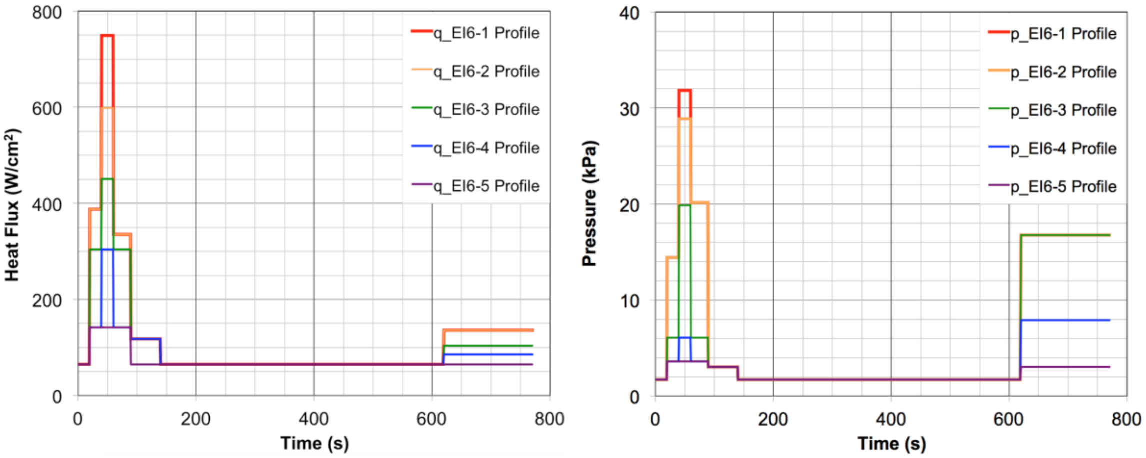

Figure 2. EI6 set of cold-wall heat flux and pressure profiles that were developed for testing.

B. Arc-Jet Facility, Test Conditions, and CFD Simulations

The 10-MW TP3 heater was selected to operate in the AHF test chamber because of its proven ability to produce heating profiles that vary as a function of time.[5] Current and mass flow rate parameters were adjusted in real-time to provide the heating profile simulations needed for these tests. A conical nozzle with a 19.05-cm (7.5-inch) diameter nozzle exit and a 5.715-cm (2.25-inch) diameter throat was used for profile testing at a wide range of facility settings. Instrumented stagnation calorimeter models and test articles were positioned 15.24 cm (6 in) from the nozzle exit for calibration and test article runs.

Slug calorimeters were used to calibrate centerline conditions for each of the seven steps of every profile at facility parameters that are summarized in Tables 1-5. Surface quantities from the slug calorimeter are shown as average values of two calorimeter measurements taken from independent runs where the calorimeter was inserted into the stream for less than 2 seconds. Subsequently, a Gardon gage calorimeter was used to verify the conditions in a continuous heating profile simulation that was carried out in a single arc-jet run. The slug calorimeter had a 10.16-cm (4-inch) diameter, flat-face geometry with r_c = 0.953 cm (0.375 in), which was the same geometry used for the test articles. The Gardon gage calorimeter also had a 10.16-cm (4-inch) diameter, flat-face geometry but with r_c = 0.160 cm (0.063 in). The independent, steady-state test conditions that were calibrated with slug calorimeters are plotted against the transient Gardon gage calorimeter measurements for every profile, as illustrated in Figs. 3-7.

Table 1. Summary of nominal facility conditions, stagnation calorimeter data, and CFD-estimated parameters for flight heating profiles EI2-1 and EI6-1.

EI2-1 / 6-1 Profile Step	I (A)	V (V)	$\dot{m}$ (g/s)	p_{midc} (kPa)	q_s (W/cm²)	p_s (kPa)	h_{ocl}, CFD (MJ/kg)	q_{HWFC}, CFD (W/cm²)
Step 1	301	1103	22	23	60	1.8	13.9	53
Step 2	1109	3244	190	203	404	14.1	30.1	362
Step 3	1807	4798	450	487	687	32.9	33.4	597
Step 4	1013	3939	321	299	336	19.5	22.7	295
Step 5	497	1469	40	40	116	2.9	20.2	103
Step 6	301	1103	22	23	60	1.8	13.9	53
Step 7	756	3726	300	246	154	16.7	12.1	122

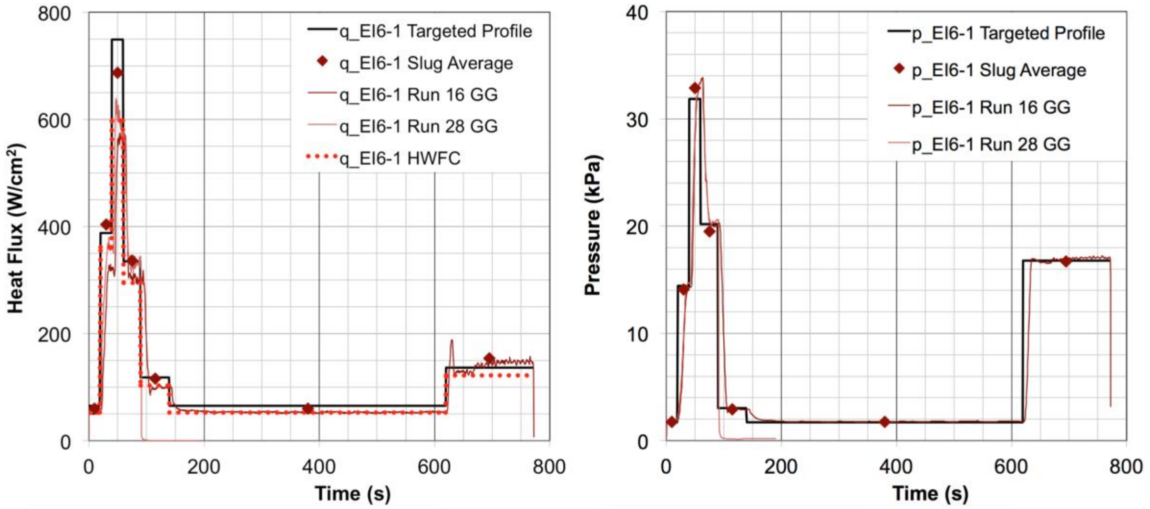

Figure 3. Slug and Gardon gage calorimeter data and computed hot-wall fully-catalytic heat flux for EI2-1 and EI6-1. Durations correspond to EI6-1 with the exception of the last two steps for Run 28.

Table 2. Summary of nominal facility conditions, stagnation calorimeter data, and CFD-estimated parameters for flight heating profiles EI2-2 and EI6-2.

EI2-2 / 6-2 Profile Step	I (A)	V (V)	$\dot{m}$ (g/s)	p_{midc} (kPa)	q_s (W/cm^2)	p_s (kPa)	h_{ocl}, *CFD* (MJ/kg)	q_{HWFC}, CFD (W/cm^2)
Step 1	301	1103	22	23	60	1.8	13.9	53
Step 2	1109	3244	190	203	404	14.1	30.1	362
Step 3	1708	4504	400	431	609	28.9	32.9	564
Step 4	1013	3939	321	299	336	19.5	22.7	295
Step 5	497	1469	40	40	116	2.9	20.2	103
Step 6	301	1103	22	23	60	1.8	13.9	53
Step 7	756	3726	300	246	154	16.7	12.1	122

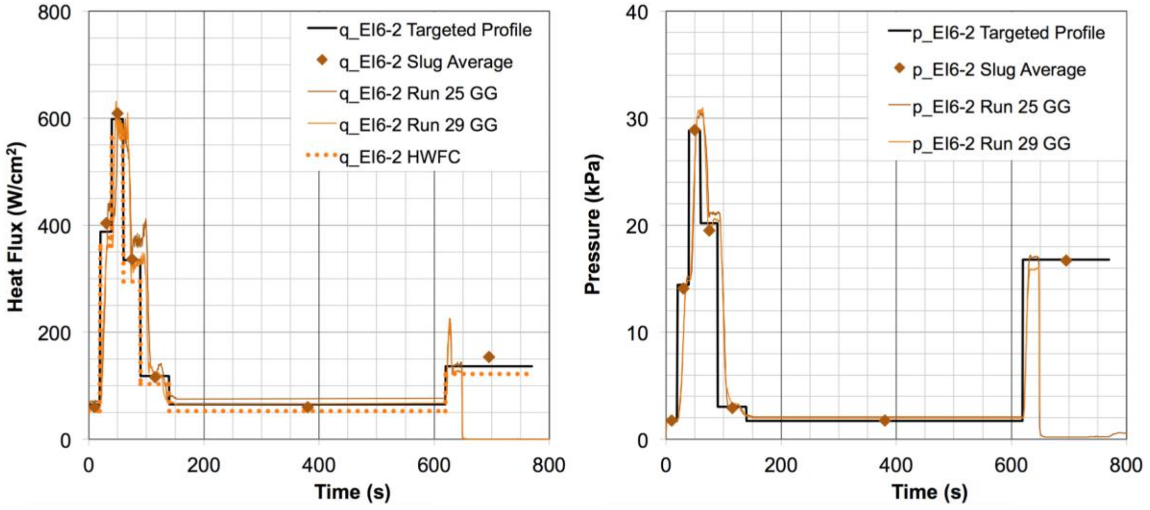

Figure 4. Slug and Gardon gage calorimeter data and computed hot-wall fully-catalytic heat flux for EI2-2 and EI6-2. Durations correspond to EI6-2 with the exception of the last step.

Table 3. Summary of nominal facility conditions, stagnation calorimeter data, and CFD-estimated parameters for flight heating profiles EI2-3 and EI6-3.

EI2-3 / 6-3 Profile Step	I (A)	V (V)	$\dot{m}$ (g/s)	p_{midc} (kPa)	q_s (W/cm^2)	p_s (kPa)	h_{ocl}, *CFD* (MJ/kg)	q_{HWFC}, CFD (W/cm^2)
Step 1	301	1103	22	23	60	1.8	13.9	53
Step 2	1009	2037	80	89	278	6.7	29.9	250
Step 3	1312	3742	269	283	463	19.4	29.8	414
Step 4	1009	2037	80	89	278	6.7	29.9	250
Step 5	497	1469	40	40	116	2.9	20.2	103
Step 6	301	1103	22	23	60	1.8	13.9	53
Step 7	840	3515	311	242	99	16.5	8.6	78

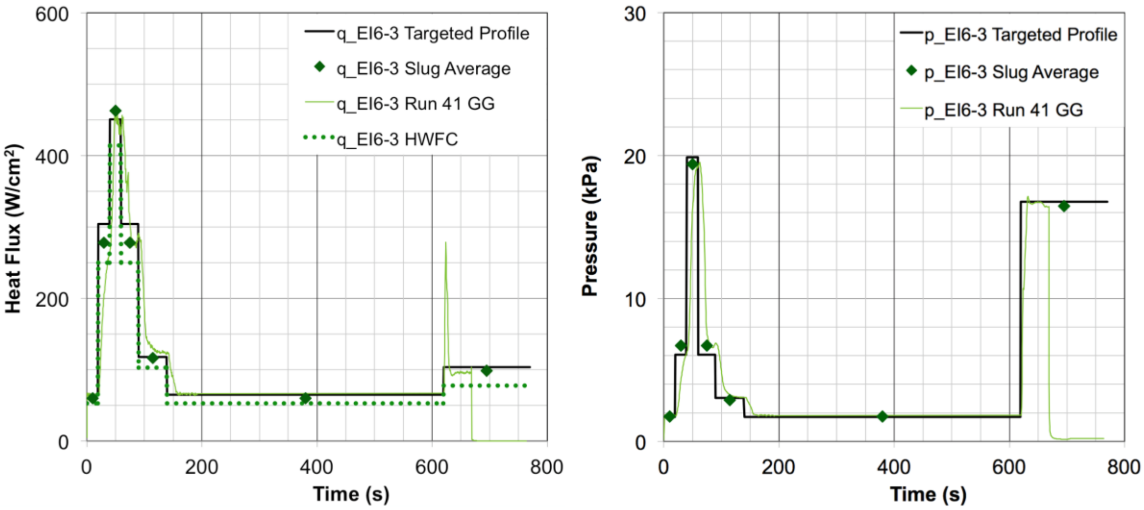

Figure 5. Slug and Gardon gage calorimeter data for EI2-3 and EI6-3. Durations correspond to EI6-3 with the exception of the last step.

Table 4. Summary of nominal facility conditions, stagnation calorimeter data, and CFD-estimated parameters for flight heating profiles EI2-4 and EI6-4.

EI2-4 / 6-4 Profile Step	I (A)	V (V)	$\dot{m}$ (g/s)	p_{midc} (kPa)	q_s (W/cm^2)	p_s (kPa)	h_{ocl}, *CFD* (MJ/kg)	q_{HWFC}, CFD (W/cm^2)
Step 1	301	1103	22	23	60	1.8	13.9	53
Step 2	730	1363	40	44	148	3.2	24.2	132
Step 3	1009	2037	80	89	278	6.7	29.9	250
Step 4	730	1363	40	44	148	3.2	24.2	132
Step 5	497	1469	40	40	116	2.9	20.2	103
Step 6	301	1103	22	23	60	1.8	13.9	53
Step 7	459	2751	142	108	82	7.6	10.0	67

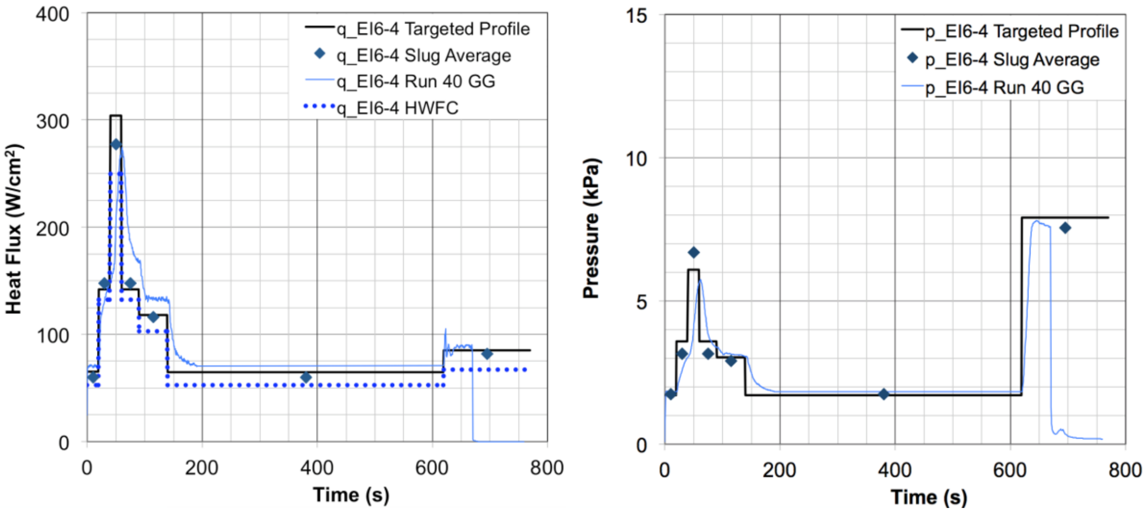

Figure 6. Slug and Gardon gage calorimeter data for EI2-4 and EI6-4. Durations correspond to EI6-4 with the exception of the last step.

Table 5. Summary of nominal facility conditions, stagnation calorimeter data, and CFD-estimated parameters for flight heating profiles EI2-5 and EI6-5.

EI2-5 / 6-5 Profile Step	I (A)	V (V)	$\dot{m}$ (g/s)	p_{midc} (kPa)	q_s (W/cm^2)	p_s (kPa)	h_{ocl}, *CFD* (MJ/kg)	q_{HWFC}, CFD (W/cm^2)
Step 1	301	1103	22	23	60	1.8	13.9	53
Step 2	730	1363	40	44	148	3.2	24.2	132
Step 3	558	1203	41	38	66	2.7	12.6	56
Step 4	301	1103	22	23	60	1.8	13.9	53
Step 5	558	1203	41	38	66	2.7	12.6	56

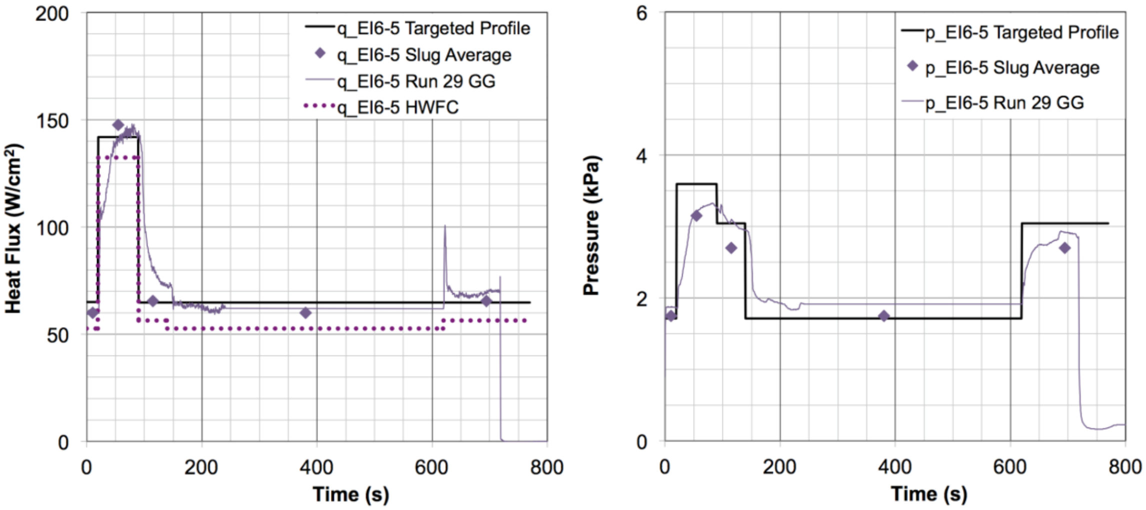

Figure 7. Slug and Gardon gage calorimeter data and computed hot-wall fully-catalytic heat flux for EI2-5 and EI6-5. Durations correspond to EI6-5 with the exception of the last step.

The Gardon gage calorimeter provided acceptable profile heat flux and pressure measurements. Each condition of every profile step was successfully achieved, and transitions between steps appeared fairly stable with the exception of the heat-flux transition to Step 7. Step 7 of every heating profile required a nitrogen injection in the plenum, referred to as add-air, to reach the achieved surface pressures while maintaining low heat flux. Since add-air typically introduces more unsteadiness in the flow compared to a simple mass flow rate adjustment, the fluctuations observed during the transition to the add-air condition were anticipated. EI2-3 and EI6-3, shown in Fig. 5, required the greatest amount of add-air of all the profiles. Consequently, these profiles exhibited the largest heat-flux variation in their ramp-up to Step 7. In any case, the excessive heat-flux variation is limited to the very beginning of Step 7, and heat flux stabilizes during the rest of the step. So, on the whole, the transient behavior exhibited during every profile was acceptably good.

In addition, the majority of the slug and Gardon gage calorimeter data are in reasonable agreement and within reasonable range of the targeted heat flux and pressure with the exception of Gardon gage heat flux for Step 3 of the highest-heating profiles, EI2-1 and EI6-1, shown in Fig. 3. On average, Gardon gage heat flux is 23% below the targeted heat flux and 16% below slug data for Step 3. Past arc-jet tests reveal that the uncertainty of stagnation heat flux measurements is within ±15% and the uncertainty of stagnation pressure measurements is within ±5%.[6] However, other recent test campaigns have suggested that the Step 3 condition may produce calibration results that are more variable than usual and may in fact be at the maximum limit of the operating envelope of the TP3 heater. Nevertheless, most of the Gardon gage and slug measurements displayed acceptable run-to-run variability for most conditions.

Computational analyses of the TP3 arc-jet tests were then performed through simulation of nonequilibrium expanding flow in the arc-jet nozzle and supersonic jet and simulation of the flow in the test box and around the test articles. For CFD calculations presented in this paper, two-dimensional axisymmetric Navier-Stokes equations, supplemented with the equations accounting for nonequilibrium kinetic processes, are used in the formulation. The thermochemical model employed for the arc-jet flow typically includes five species (N_2 O_2, NO, N, O), though six species are included when argon is present for Step 1 and Step 5. The thermal state of the gas is described by two temperatures (translational-rotational and vibrational-electronic) within the framework of Park's two-temperature model. Based on the computational approach that follows our earlier work,[5, 7] the simulations of the TP3 arc-jet facility flow are started from the nozzle inlet. The total enthalpy and its radial profile at the inlet are prescribed based on the facility and calibration data, and the flow properties at the inlet are assumed to be in thermochemical equilibrium. Measured facility data, namely, the total pressure, mass flow rate, and test box pressure, are used as boundary conditions.

The primary objective of the CFD simulations is to estimate the centerline total enthalpy of the arc-jet flow consistent with the facility and cold-wall calorimeter measurements. As an illustration of a typical CFD simulation, Fig. 8 shows a computed TP3 19.05-cm (7.5-inch) nozzle flowfield including the test box and a stagnation calorimeter model. In order to estimate the centerline enthalpy of the flow, uniform pressure and a nonuniform parabolic enthalpy profile are specified at the nozzle inlet such that the centerline calibration data are reproduced with the computations. Similarly, CFD analyses are used to calculate hot-wall fully-catalytic heat flux, which is illustrated in Figs. 3-7. Tables 1-5 also list the CFD-estimated centerline total enthalpy and hot-wall heat flux values that correspond to the arc-jet facility and calibration data for each flight heating profile simulation.

The aerothermal flight environments were first predicted by the Orion CEV Aerosciences Project (CAP) team assuming fully catalytic radiative equilibrium boundary conditions; and cold-wall heating profiles (shown in Figs. 1-2) were derived from these predictions. Since the cold-wall heat flux to hot-wall heat flux conversions are different for flight and arc-jet environments, CFD simulations are also used to provide hot-wall fully-catalytic heat flux estimates for all of the heating profiles tested. For traceability of the material performance in arc-jet tests to flight, comparisons of hot-wall fully-catalytic heat flux profiles are relevant. In the present paper, although such comparisons are not made, CFD-predicted hot-wall fully-catalytic heat flux profiles are provided for future comparisons.

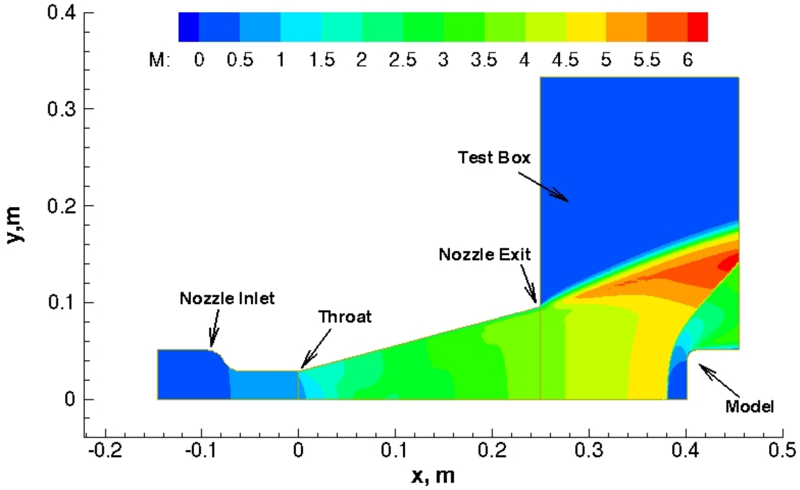

Figure 8. Computed Mach number contours of the TP3 19.05-cm (7.5-inch) nozzle flowfield including the test box and a 4-inch diameter flat-faced calorimeter model: $\dot{m}$ = 190 g/s, h_{ob} = 17.6 MJ/kg, h_{ocl} = 28.8 MJ/kg.

C. Fencing Measurements

In general, fencing and its inverse, gapping, are defined by the difference between Avcoat recession and recession in the RTV gap filler. Because each model was tested over a series of environments, as described above, and the ablative response of molded Avcoat and RTV can vary depending on the environment, it was essential to determine recession throughout the model run to understand how the different conditions of each profile influenced fencing. Therefore, time-varying recession measurements of test articles were collected during the model runs via the photogrammetric recession measurement (PRM) technique to determine surface recession across test duration for every profile. PRM analysis additionally enabled fencing heights and rates to be evaluated for every step of each profile. Meanwhile, recession analysis of pre-test and post-test laser scans was used to independently determine post-test fencing and validate post-test values from PRM data.

PRM, an imaging method developed at NASA ARC, relies on cross-correlating images from two synchronized high-resolution video cameras to measure recession.[8] Cameras were positioned behind the top and west port windows of the test chamber and captured images of the test article via angled mirrors that were installed adjacent to the nozzle exit. Ideally, a point-matching algorithm would be used to ensure that the two different cameras were identifying recession at the same pre-determined points throughout the surface of the model and throughout the duration of the test. However, the test articles assessed in this test series challenged the robustness of target-finding algorithms. The topography of every model exhibited spatial and temporal variations, and the 3-dimensionality of the dynamic glass melt that appeared on the surface made consistent point tracking and recession evaluation problematic. Consequently, the reported measurements were limited to locations closest to the centerline that were identified as appropriate for analysis based on user input. Generally, points that were considered representative of the center of the model at the gap and neighboring Avcoat were chosen.

Meanwhile, there were no issues collecting laser scans before and after testing using a high-speed 3D laser scanner that was also developed at NASA ARC.[9] Hence, determining recession and then fencing of every model from the difference between the pre-test and post-test laser scans was straightforward.

III. Test Results

A. Fencing Developments

One molded Avcoat test article with a 2.0-mm (0.08-inch) wide gap filled with RTV was tested for every profile with the gap filler oriented horizontally. All test articles were flat-face and had a diameter of

10.16 cm (4 in), thickness of 3.81 cm (1.5 in), and r_c of 0.953 cm (0.375 in). All models employed Avcoat collars to reduce the effects of sidewall heating on the gap feature. A typical test article shown before and after testing is exhibited in Fig. 9. During the course of testing, the longer, higher-heating profiles—EI6-1, EI6-2, and EI6-3—were cut short at the last step since the real-time video feed revealed the onset of collar failure. Instead of testing for the full duration of 770 seconds, the EI6-1 profile was reduced to 660 seconds, and the EI6-2 and EI6-3 profiles were reduced to 700 seconds. Nevertheless, the data obtained from these profiles still provide meaningful results regarding fencing.

Although each profile varied in heat flux and pressure, the overall surface response of every test article is broadly similar and is demonstrated by the sequence of video stills in Fig. 10. During the first heat pulse consisting of Steps 1 through 5, uniform Avcoat recession was observed while the gap filler receded slightly below the Avcoat surface, revealing gapping behavior. During the dwell at Step 6, there was swelling of the silica and controlled recession away from the gap. And during the second high-pressure pulse at Step 7, excessive swelling of the entire surface was followed by rapid recession as fencing developed due to the gap filler receding slower than the surrounding Avcoat.

Figure 9. Pre-test and post-test photographs of the flat-face Avcoat test article with 2.0-mm RTV gap tested at the EI6-1 profile for 660 seconds.

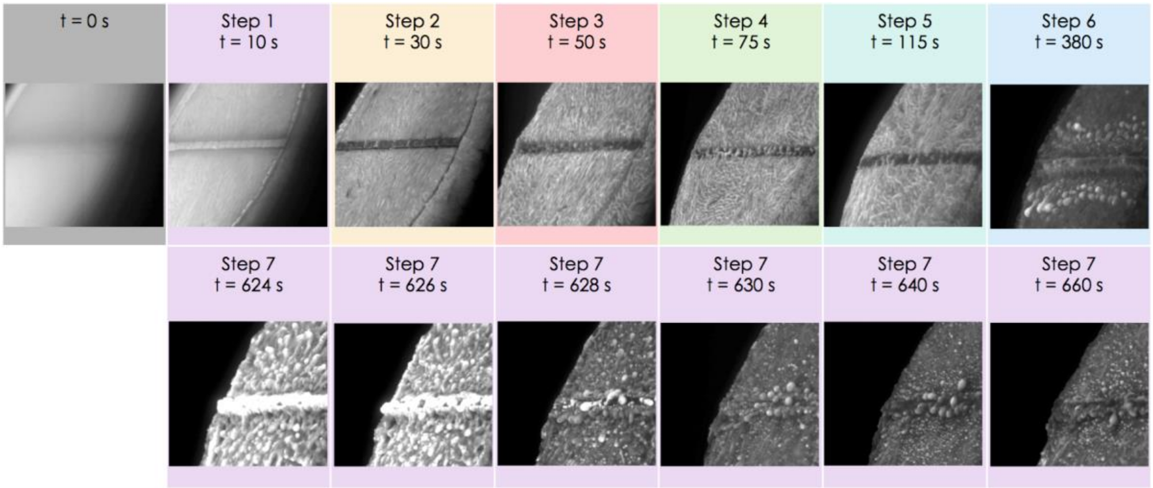

Figure 10. Video stills of EI6-1 test article demonstrating the progression of surface response.

Such qualitative observations are quantified by the differential recession measurements that were collected via PRM and laser scans. For PRM, differential recession throughout the duration of each profile was determined from Avcoat and gap-filler recession at locations nearest the model centerline that were characteristic of the gap filler and neighboring Avcoat. Recession data within the selected gap-filler and

Avcoat regions of interest were averaged and, whenever the surface displayed excessive dynamic behavior (as demonstrated in Step 7 of Fig. 10), the recession regions of interest were deliberately modified to avoid biasing differential recession toward features that misrepresented the data. An example of PRM data and differential recession results is illustrated for EI6-1 in Fig. 11. Note that the discontinuities in the differential recession results corresponding to Step 3 (near t = 30 seconds) and the ramp-up to Step 7 (near t = 620 seconds) originated from the break in the gap-filler data that developed when the model surface behavior made it too difficult to reliably discern recession at these points in time. In summary, the PRM results represent the best attempts to combine recession across different segments of time and space for every profile test article.

Meanwhile, post-test fencing was assessed from laser scans in a more consistent manner by analyzing the recession along linecuts that were perpendicular to the gaps and located at the centerline of each model, as shown in Fig. 12a. Recession at the gap filler was observed at the region located ±5-mm from the centerline, and recession at the neighboring Avcoat was observed within the 10-mm regions above and below the defined gap-filler region, as illustrated in Fig. 12b. Average fencing was determined from the difference between the mean Avcoat recession and minimum gap-filler recession. Maximum fencing was assessed from the difference between minimum Avcoat recession and minimum gap-filler recession, and minimum fencing was evaluated from the difference between maximum Avcoat recession and minimum gap-filler recession.

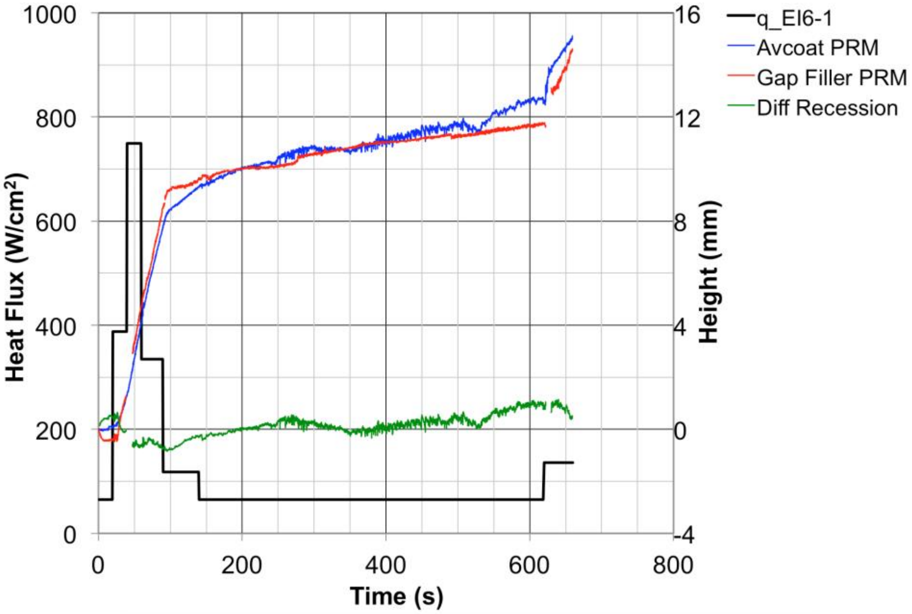

Figure 11. PRM and differential recession results for EI6-1 test article plotted against heat flux profile for reference.

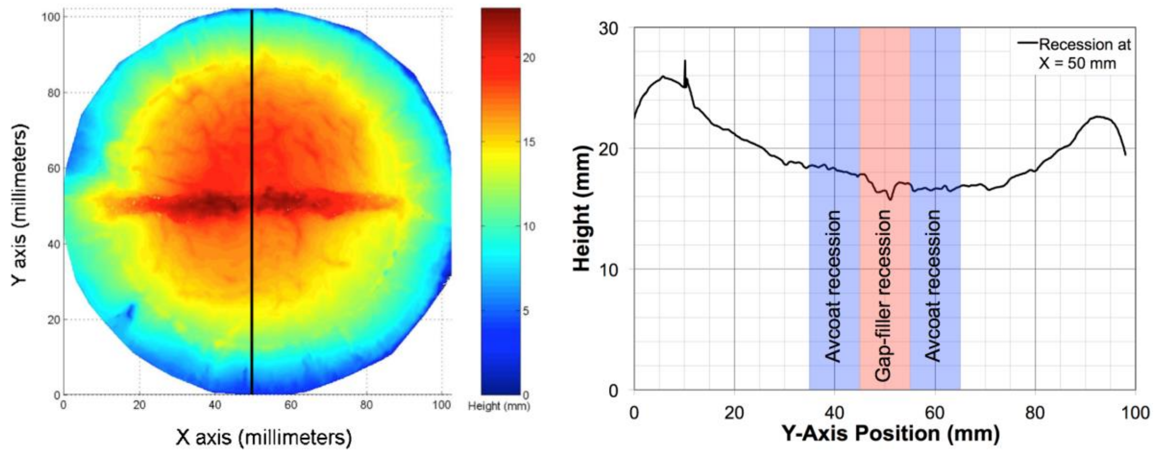

(a) **(b)**

Figure 12. Laser scan results used to evaluate post-test fencing for EI6-1 test article. (a) Post-test laser scan with linecut at x = 50 mm, indicating location of recession and fencing analysis. (b) Recession plot with colored regions denoting which points were used to analyze gap-filler and Avcoat recession and subsequent fencing.

The fencing results from the PRM and laser scans (average, maximum, and minimum post-test fence heights) are presented in Figs. 13-17. The results from every profile illustrate that a small amount of fencing occurred during the first, low-heating step of each profile. However, once heat flux increased beyond 150 W/cm^2—as it did by Step 2 of the high-heating profiles displayed in Fig. 13-15 and by Step 3 of the moderate heating profiles shown in Fig. 16—gapping ensued during the rest of the first pulse. Gapping corresponded to a surface temperature range of about 1800^{o}C-2300^{o}C, as measured by a dual-wavelength optical pyrometer that was pointed at the center of the test articles. While the PRM data reveal the development of a shallow cavity less than 2-mm for all gapping instances, the video footage visibly demonstrates that the resulting cavity does not widen during the gapping stage at higher heat fluxes. Note that incomplete PRM data are shown in Fig. 15 because video-recording difficulties occurred throughout most of EI2-3. Results from EI2-4 and EI6-4 in Fig. 16 also suggest that gapping is less pronounced in depth and duration at more moderate heat fluxes as evidenced by the displayed gap development, which is shallower and briefer than the gapping shown at the higher-heating profiles. The PRM data in Fig. 17 show that gapping never develops at heat fluxes below 150 W/cm^2, which corresponds to a surface temperature range of about 1200^{o}C-1800^{o}C. RTV receded minimally while Avcoat experienced significant recession that was primarily driven by glass melt at these sufficiently low heating rates and surface temperatures. Thus, only fencing occurred throughout the first pulse of the lowest-heating profiles. Although the gapping clearly delayed fencing at the higher-heating profiles, moderate fencing inevitably followed during the dwell of every profile. Lastly, the second heat pulse exacerbated the fencing at every profile resulting in maximum fence heights between 4-mm and 6-mm for models that were tested at the full duration.

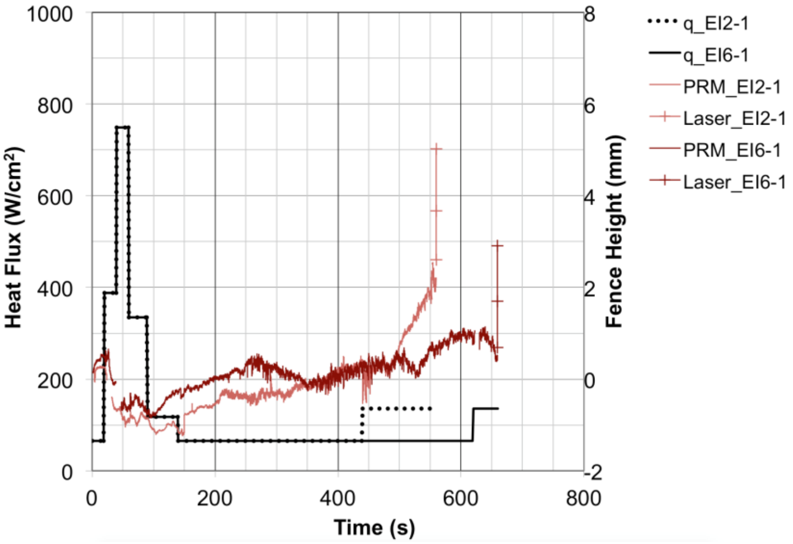

Figure 13. EI2-1 and EI6-1 fencing profiles and post-test fencing results plotted against heating profiles for reference.

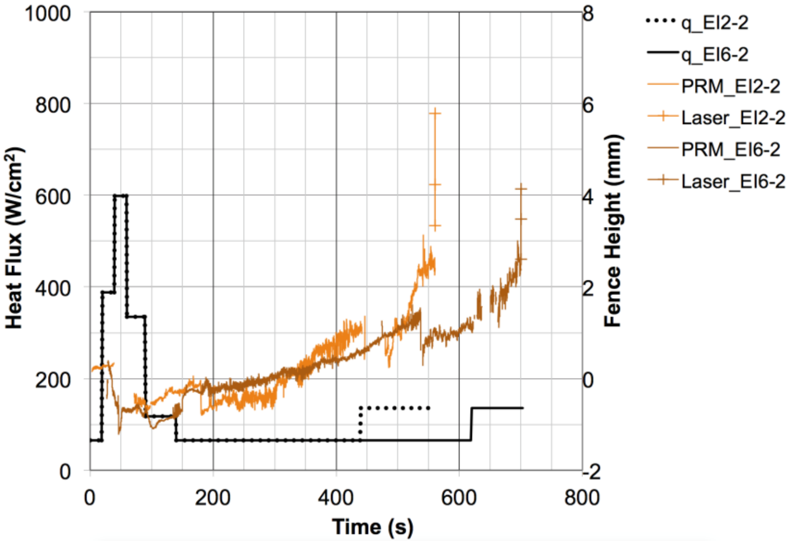

Figure 14. EI2-2 and EI6-2 fencing profiles and post-test fencing results plotted against heating profiles for reference.

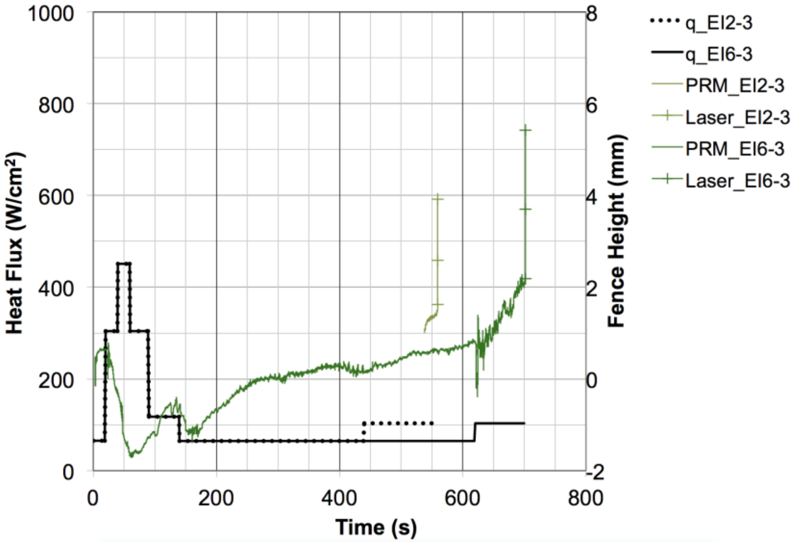

Figure 15. EI2-3 and EI6-3 fencing profiles and post-test fencing results plotted against heating profiles for reference.

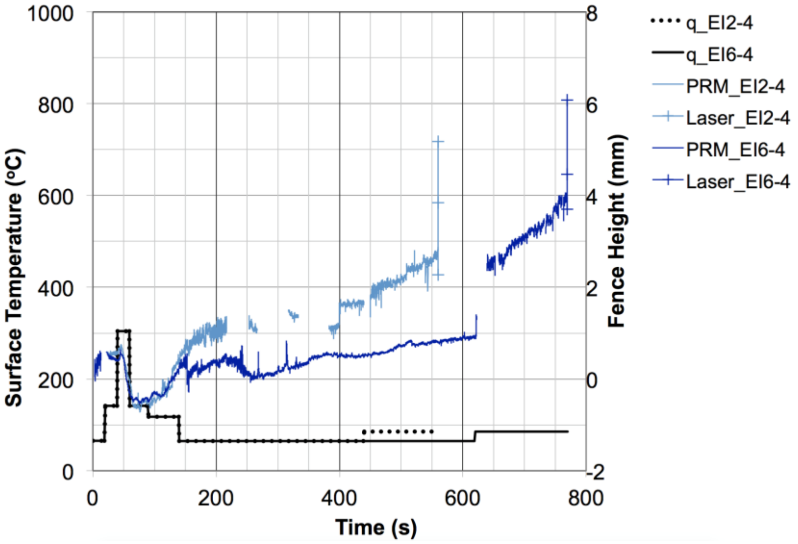

Figure 16. EI2-4 and EI6-4 fencing profiles and post-test fencing results plotted against heating profiles for reference.

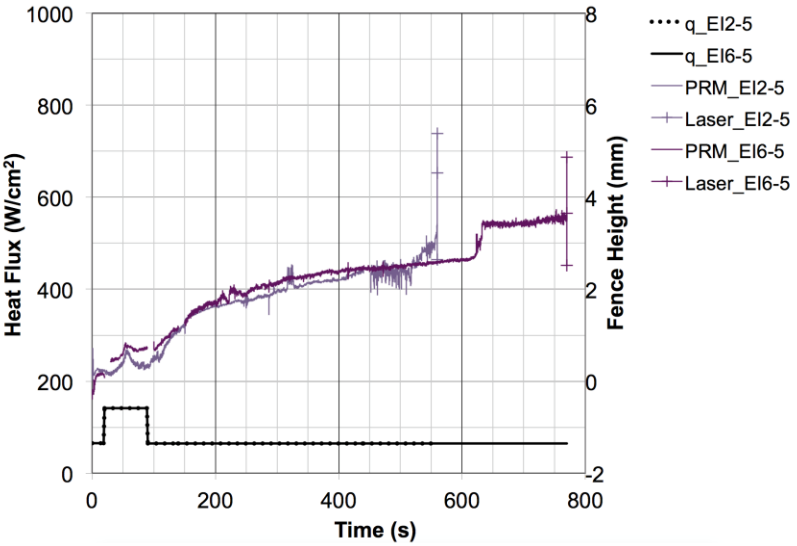

Figure 17. EI2-5 and EI6-5 fencing profiles and post-test fencing results plotted against heating profiles for reference.

PRM data at the end of the test are bounded by the minimum and maximum fence heights determined from laser scans. However, average fence height from laser scans is consistently greater than post-test fence height by PRM. This is mostly because different regions were selected for fencing evaluation under each method. The user guidance required to evaluate PRM data from this test series introduced uncertainty that is greater than ±0.2-mm, which is the uncertainty expected for measurements obtained at positions tracked by traditional algorithms. Meanwhile, laser scan measurements have an uncertainty of ±0.5-mm, and the laser scan method of determining fencing is more rigorous and repeatable than the PRM method discussed. Therefore, PRM data were used to model environment-dependent fencing behavior while the laser scans were used to anchor the fencing rates determined by PRM to ultimately create an empirically-based set of conservative, temporal fencing profiles for heatshield sizing inputs.

IV. Summary

This paper describes arc-jet test results for the characterization of fencing development. The 10-MW TP3 arc heater in the AHF at NASA ARC was successfully leveraged for its heating-profile testing capability to simulate various EM-1 profiles that are traceable to different regions of the heatshield. A molded Avcoat coupon with an RTV gap, serving as a model for the tiled Orion TPS design, was exposed to every heating profile, during which differential recession measurements were captured. PRM helped to observe the timing and extent of the resulting protuberances in stagnation, which enabled the modeling of fencing behavior at various heating profiles and provided the coupled fencing and environment inputs required for sizing of the EM-1 heatshield. PRM data reveal that gapping occurs above 150 W/cm^2, and the presence of gapping attenuates fencing behavior. In all heating profiles used for testing, the gap filler ultimately protrudes above the molded Avcoat, up to 6 mm for the worst case. This resulting fencing is typically associated with augmented heating and accelerated boundary layer transition to turbulence. However, fencing is suspected to be reduced in shear since the gap filler is not as robust under shear stress. Therefore, additional testing is currently being pursued in a wedge configuration to observe the effect shear has on differential recession and determine the degree of conservatism that has been applied to the current fencing models.

Acknowledgments

The authors gratefully acknowledge the support provided by the Orion TPS Insight and Oversight Project and NASA ARC Entry Systems and Technology Division through their NNA10DE12C to ERC Incorporated and NNA15BB15C to AMA Incorporated. The authors would also like to thank Kathy McGuire and Alvaro Rodriguez (JSC), who developed the heating profiles that were the basis of this work; the PRM team—Edward Schairer, Laura Kushner, and JT Heineck; the arc-jet test facility team at Ames—in particular Tien Nguyen and Charlene Conlan; and NASA-SCAP for their critical financial support of the arc-jet operational capability at Ames.

References

---

[1] Cichan, T., Norris, S.D., and Marshall, P.F., "Orion: EFT-1 Flight Test Results and EM-1/2 Status," AIAA Paper 2015-4414, August 2015.

[2] Beck, R.A.S., Driver, D.M., Wright, M.J., Hwang, H.H., Edquist, K.T., Sepka, S.A., "Development of the Mars Science Laboratory Heatshield Thermal Protection System," *Journal of Spacecraft and Rockets*, Vol. 51, No. 4, 2014, pp. 1139-1150.

[3] Tang, C., Edquist, K.T., Wright, M.J., Sepka, S.A., and Cassel, A., "Numerical Simulations of Protruding Gap Fillers on the Mars Science Laboratory Heatshield," AIAA Paper 2009-4077, June 2009.

[4] Driver, D.M., Carballo, E., Beck, R.A.S., Prabhu, D., Santos, J.A., Cassell, A., Skokova, K., Tang, C., Hwang, H.H., Slimko, E., Willcockson, W., Songer, J., "Arc Jet Testing in a Shear Environment for Mars Science Laboratory Thermal Protection System," AIAA Paper 2009-4230, June 2009.

[5] Balboni, J.A., Gökçen, T., Hui, F.C.L., Graube, P., Morrissey, P., and Lewis, R., "Consolidating NASA's Arc Jets," AIAA Paper 2015-2667, June 2015.

[6] Covington M.A, Heinemann, J.M., Goldstein, H.E., Chen, Y.-K., Terrazas-Salinas, I., Balboni, J.A., Olejniczak, J., and Martinez, E.R., "Performance of a Low Density Ablative Heat Shield Material," *Journal of Spacecraft and Rockets*, Vol. 45, No. 2, 2008, pp. 237-247.

[7] Gökçen, T., Balboni, J.A., and Alunni, A.I. "Computational Simulations of the 10-MW TP3 Arc-Jet Facility," AIAA Paper 2015-3103, June 2015.

[8] Schairer, E.T. and Heineck, J.T., "Photogrammetric Recession Measurements of Ablative Materials in Arcjets," *Measurement Science and Technology*, Vol. 21, No. 2, 2010.

[9] Lavelle, J.P., Schuet, S.R., and Schuet, D.J., "High Speed 3D Scanner with Real-Time 3D Processing," IEEE 0-7803-8591, 2004.